THE ASTROPHYSICAL JOURNAL, 517:977–989, 1999 June 1

DECONVOLUTION OF DIRECTLY PRECIPITATING AND TRAP-PRECIPITATING ELECTRONS IN SOLAR FLARE HARD X-RAYS. III. *YOHKOH* HARD X-RAY TELESCOPE DATA ANALYSIS

MARKUS J. ASCHWANDEN AND LYNDSAY FLETCHER
Lockheed-Martin ATC, Solar and Astrophysics Laboartory, Department L9 41, Building 252, 3251 Hanover Street, Palo Alto, CA 94304; aschwanden@sag.lmsal.com

TARO SAKAO
National Astronomical Observatory, Mitaka, Tokyo 181-8588, Japan

TAKEO KOSUGI
Institute of Space and Astronautical Science, 3-1-1 Yoshinodai, Sagamihara, Kanagawa 229-8510, Japan

AND

HUGH HUDSON
Solar Physics Research Corporation, Tucson, AZ 85718
Received 1998 October 13; accepted 1999 January 4

ABSTRACT

We analyze the footpoint separation d and flux asymmetry A of magnetically conjugate double footpoint sources in hard X-ray images from the *Yohkoh* Hard X-Ray Telescope (HXT). The data set of 54 solar flares includes all events simultaneously observed with the *Compton Gamma Ray Observatory* (*CGRO*) in high time resolution mode. From the *CGRO* data we deconvolved the direct-precipitation and trap-precipitation components previously (in Paper II). Using the combined measurements from *CGRO* and HXT, we develop an asymmetric trap model that allows us to quantify the relative fractions of four different electron components, i.e., the ratios of direct-precipitating (q_{P1}, q_{P2}) and trap-precipitating electrons (q_{T1}, q_{T2}) at both magnetically conjugate footpoints. We find mean ratios of $q_{P1} = 0.14 \pm 0.06$, $q_{P2} = 0.26 \pm 0.10$, and $q_T = q_{T1} + q_{T2} = 0.60 \pm 0.13$. We assume an isotropic pitch-angle distribution at the acceleration site and double-sided trap precipitation ($q_{T2}/q_{T1} = q_{P2}/q_{P1}$) to determine the conjugate loss-cone angles ($\alpha_1 = 42^\circ \pm 11^\circ$ and $\alpha_2 = 52^\circ \pm 10^\circ$) and magnetic mirror ratios at both footpoints ($R_1 = 1.6, \ldots, 4.0$ and $R_2 = 1.3, \ldots, 2.5$). From the relative displacement of footpoint sources we also measure altitude differences of hard X-ray emission at different energies, which are found to decrease systematically with higher energies, with a statistical height difference of $h_{\rm Lo} - h_{M1} = 980 \pm 250$ km and $h_{M1} - h_{M2} = 310 \pm 300$ km between the three lower HXT energy channels (Lo, M1, M2).

Subject headings: acceleration of particles — radiation mechanisms: nonthermal — Sun: corona — Sun: flares — Sun: X-rays, gamma rays

1. INTRODUCTION

Hard X-ray (HXR) images of solar flares often show double sources that have been interpreted as precipitation sites of nonthermal electrons at magnetically conjugate footpoints of dipolar loop structures (e.g., Duijveman, Hoyng, & Machado 1982; Nitta, Dennis, & Kiplinger 1990; Sakao 1994). These HXR double footpoint sources often have asymmetric fluxes and require therefore an asymmetric coronal magnetic field (assuming equal coronal densities at the footpoints). Conservation of the magnetic moment ($\mu \propto \sin^2 \alpha/B$) tells us that the pitch angle α of a free-streaming electron is directly related to the local magnetic field B. Even if the electron is not free streaming, an immediate consequence of this relation is that the precipitating electron rate, and thus the resulting thick-target HXR flux, is higher at the footpoint with the weaker magnetic field, whereas emission from trapped electrons (e.g., gyrosynchrotron emission) is higher at the opposite footpoint with the stronger magnetic field, due to the higher trapping efficiency there, also referred to as "*cornucopia model*" (Li et al. 1997). This complementarity of conjugate HXR sources and their counterweighted microwave emission has been observationally verified (e.g., by Wang et al. 1995; Hanaoka 1997), but no quantitative models of asymmetric traps have been developed yet. Here we measure the asymmetry of conjugate HXR sources and use it to model the asymmetric magnetic field and the resulting properties of asymmetric electron traps, using HXT images from *Yohkoh*, in conjunction with trapping parameters determined previously from *Compton Gamma-Ray Observatory* (*CGRO*).

Why is the consideration of asymmetric magnetic fields important for modeling of solar flares? Most flare models are based on a single symmetric loop, from which the emission of precipitating and trapped electrons is calculated, including their relative timing and their HXR and microwave spectra. However, the trapped component is considerably delayed with respect to the direct-precipitation component, and the spectrum of trapped electrons is expected to be significantly harder because of the longer collisional deflection time of high-energy electrons ($\tau_{\rm Defl} \propto E^{3/2}$). Therefore, depending on the relative contributions of direct- and trap-precipitating electrons, the timing and spectra at two conjugate footpoints are generally different. This disparity of HXR and/or microwave spectra at conjugate footpoints has been noticed in several studies (e.g., Sakao 1994; Wang et al. 1995). The relative timing of conjugate HXR footpoints has been found to be nearly simultaneous, within an uncertainty of 0.1–0.3 s (Sakao 1994), and even less uncertainty in a revised analysis. Although this simultaneity is expected for the direct-precipitation component, if the accelerator is located halfway between the two

footpoints, it cannot easily be understood for the trap-precipitation component in an asymmetric trap, unless the relative weighting of direct-precipitating and trap-precipitating components is delicately balanced at the two footpoints. This balance has not been demonstrated yet, either observationally or theoretically. It was not until this study that we had all of the data needed to address the problem. Given the complexity of four electron components with different timing and spectra (i.e., a direct-precipitation and trap-precipitation component at each footpoint), which are all superposed in a single HXR spectrum obtained from nonimaging data, previous theoretical modeling of such single HXR spectra and their characterization with a single spectral index must be considered as a highly oversimplified and questionable approach. In this study we attempt for the first time to separate these four electron components by quantifying their relative contributions and the associated asymmetric magnetic fields in flare loops.

In § 2 we analyze the footpoint separation and asymmetry of magnetically conjugate double sources observed with *Yohkoh*/HXT. In § 3 we develop an asymmetric trap model that allows us to quantify the relative fractions of direct-precipitating and trap-precipitating electrons at both footpoints from combined HXT and *CGRO* data. Conclusions are summarized in § 4.

2. *YOHKOH*/HXT DATA ANALYSIS

We analyze HXR images from the Hard X-Ray Telescope (HXT) (Kosugi et al. 1991) on board the *Yohkoh* satellite, which takes images in four energy ranges (Low, 14–23 keV; M1, 23–33 keV; M2, 33–53 keV; High, 53–93 keV) and has a spatial resolution of $\gtrsim 5''$, with a time cadence of 0.5 s in flare mode. Observational information on flares detected with HXT, such as time profiles, the peak count rates in the four energy channels, the heliographic flare positions, or the associated NOAA active region numbers and *GOES* flare classifications are compiled in The *Yohkoh* HXT Databook (I) (Kosugi et al. 1993).[1]

From the data set of 140 flares simultaneously observed with the Burst and Transient Source Experiment (BATSE) on board the *Compton Gamma Ray Observatory* (*CGRO*) with high (64 ms) time resolution and with *Yohkoh* in flare mode, HXT data were available for 84 flare events. Among them, we were able to reconstruct HXR images for 77 flares with the maximum entropy method (MEM), with reasonable quality for source structure analysis. The main objective of this study requires the measurement of the separation distance and the relative fluxes of conjugate footpoints of the primary HXR flare loops. A double footpoint structure could be resolved in 54 events (Table 1), whereas the remaining 23 events showed an unresolved single source or unresolved components near the solar limb. The verification of conjugate footpoints is also based on simultaneous SXR images from the Soft X-Ray Telescope (SXT), which are shown in coalignment with HXT images in an earlier study (Aschwanden et al. 1996b, 1996c).

2.1. *Measurement of Footpoint Separation*

We use the same HXT images of an earlier study (Aschwanden et al. 1996b), which have been integrated over time intervals carefully synchronized with the analyzed intervals of BATSE/*CGRO* high time resolution medium energy resolution (MER) data, covering typically ≈ 1–3 minutes after the beginning of the HXR impulsive flare phase (as detected by the *CGRO* burst trigger criterion).

To measure the footpoint separation and their relative fluxes we have chosen the simple method of fitting a two-Gaussian model to the conjugate footpoint sources in the HXT images. Such a source model map,

$$F^{\rm model}(x, y) = f_1 \exp\left[-\frac{(x - x_1)^2 + (y - y_1)^2}{2w_1^2} \right] + f_2 \exp\left[-\frac{(x - x_2)^2 + (y - y_2)^2}{2w_2^2} \right] \quad (1)$$

is parametrized with eight free parameters, the center locations (x_1, y_1) and (x_2, y_2) of the two footpoints, their fluxes f_1 and f_2, and their Gaussian widths w_1 and w_2. We used a standard minimization algorithm (available in the IDL software) based on the Powell method (Press et al. 1986) to fit the two-dimensional model map (eq. [1]) to the observed HXT images by minimizing the sum of the least-square deviations in map subareas that cover the two conjugate footpoints. From the positions of the HXR flare footpoints (x_i, y_i) relative to the Sun center (x_0, y_0) we determine the heliographic coordinates (l_1, b_1) and (l_2, b_2) of the two footpoints (the heliographic coordinate transformations are given in Appendix A in Aschwanden et al. 1999) and calculate their separation distance d on the solar surface,

$$d = 2\pi R_\odot \frac{\sqrt{[(l_1 - l_2)\cos b_1]^2 + (b_1 - b_2)^2}}{360^\circ}, \quad (2)$$

with $R_\odot = 696$ Mm. The HXT maps of the highest energy channels in which the double footpoint structure is clearly identifiable are shown in Figure 1 and the corresponding two-Gaussian fits in Figure 2. The derived footpoint distances d are listed for all 54 flares in Table 1, evaluated in those energy channels (Lo, M1, M2) where a consistent footpoint morphology was apparent.

2.2. *Asymmetry of Hard X-Ray Footpoint Sources*

We define the asymmetry ratio A of the HXR fluxes f_1 and f_2 at the two conjugate footpoints by the normalized ratio of the stronger footpoint source f_2,

$$A \equiv \frac{f_2}{(f_1 + f_2)}, \quad f_1 < f_2 . \quad (3)$$

With this definition, the asymmetry ratio varies from $A = 0.5$ for symmetric footpoints to $A = 1.0$ for maximum asymmetry (one-sided footpoint). The asymmetry of the HXR fluxes is visualized in Figure 3, where a flux profile in each HXT image is interpolated along a baseline that intersects the two footpoint positions (x_1, y_1) and (x_2, y_2). We caution that apparent double sources could potentially consist of unresolved multiple footpoint sources. For completeness we mention also that Sakao (1994) used a different method to measure HXR fluxes of double footpoint sources by convolving Gaussian source components with the instrumental modulation pattern. Also, note that the improved HXT modulation pattern determined by Sato, Kosugi, & Makishima (1999) is not applied here.

[1] http://solar.nro.nao.ac.jp/~hxthome/.

TABLE 1

PARAMETERS MEASURED FROM HXT AND *CGRO* IN 54 SOLAR FLARES

BATSE Burst Number	Date	Start Time (UT)	Footpoint Distance d (Lo, M1, M2) (Mm)	Time-of-Flight Distance l^{TOF} (Mm)	Flux Asymmetry A (Lo, M1, M2)	Precipitation Fraction q	References
876	1991 Oct 07	1016:11	6.6, ..., ...	...	0.51, ..., ...	0.35 ± 0.2	1
972	1991 Oct 31	0909:05	15.5, 15.8, ...	11 ± 4	0.44, 0.56, ...	0.40 ± 0.1	1
1032	1991 Nov 09	2052:03	13.9, 10.9, ...	21 ± 9	0.75, 0.73, ...	0.20 ± 0.1	1
1037	1991 Nov 10	2006:39	..., 24.2, 24.1	28 ± 3	..., 0.64, 0.52	0.30 ± 0.1	1
1055	1991 Nov 13	2115:55	15.8, 14.8, ...	13 ± 2	0.85, 0.70, ...	0.60 ± 0.1	1
1066	1991 Nov 15	2234:39	27.6, 25.2, ...	16 ± 4	0.48, 0.50, ...	0.50 ± 0.1	1, 2
1089	1991 Nov 19	0928:29	19.5, 19.2, ...	...	0.25, 0.51, ...	0.51 ± 0.2	1
1146	1991 Dec 04	1743:10	24.7, 23.4, ...	22 ± 5	0.71, 0.61, ...	0.40 ± 0.1	1, 2
1151	1991 Dec 07	2152:46	31.7, ..., ...	20 ± 7	0.61, ..., ...	0.50 ± 0.1	1
1164	1991 Dec 12	1705:16	28.5, 30.1, ...	...	0.78, 0.76, ...	0.45 ± 0.3	1
1169	1991 Dec 14	0548:43	10.4, 9.8, ...	15 ± 5	0.53, 0.78, ...	0.40 ± 0.1	1
1181	1991 Dec 15	1832:33	..., 11.1, ...	15 ± 2	..., 0.62, ...	0.60 ± 0.1	1
1183	1991 Dec 16	0101:33	8.5, 10.7, ...	10 ± 5	0.46, 0.70, ...	0.20 ± 0.1	1
1184	1991 Dec 16	0455:55	20.9, 22.7, 22.9	36 ± 16	0.57, 0.51, 0.47	0.10 ± 0.1	1, 2
1220	1991 Dec 25	1254:12	..., 18.4, ...	12 ± 4	..., 0.53, ...	0.20 ± 0.1	1
1227	1991 Dec 26	1048:02	..., 9.7, ...	...	..., 0.69, ...	0.47 ± 0.3	1
1234	1991 Dec 26	2136:34	..., 41.6, 40.6	58 ± 7	..., 0.93, 0.93	0.60 ± 0.1	1
1243	1991 Dec 28	1226:32	..., 13.0, 12.0	...	..., 0.67, 0.72	0.42 ± 0.3	1
1252	1991 Dec 30	2306:50	..., 13.7, ...	...	..., 0.56, ...	...	
1260	1992 Jan 01	0306:51	23.9, 25.7, ...	...	0.65, 0.57, ...	...	
1296	1992 Jan 13	1727:28	23.3, 28.9, 21.7	42 ± 9	0.59, 0.55, 0.56	0.30 ± 0.1	1, 3
1341	1992 Feb 03	0045:02	15.8, 11.1, ...	16 ± 5	0.54, 0.73, ...	0.30 ± 0.1	1
1343	1992 Feb 03	0658:34	6.9, ..., ...	14 ± 3	0.52, ..., ...	0.40 ± 0.1	1
1356	1992 Feb 05	0642:53	..., 13.8, ...	...	..., 0.72, ...	0.54 ± 0.3	1
1361	1992 Feb 06	0315:48	..., ..., 30.6	...	..., ..., 0.19	0.32 ± 0.2	1
1366	1992 Feb 07	0342:50	16.0, 15.9, 20.0	16 ± 5	0.48, 0.55, 0.74	0.40 ± 0.1	1, 2
1371	1992 Feb 08	0722:10	..., 12.1, ...	...	..., 0.73, ...	0.42 ± 0.3	1
1398	1992 Feb 14	2307:20	21.7, 24.1, 23.7	28 ± 11	0.58, 0.59, 0.66	0.20 ± 0.1	1
1400	1992 Feb 15	0836:15	11.7, 12.7, ...	48 ± 18	0.52, 0.66, ...	0.20 ± 0.1	1
1411	1992 Feb 17	1540:23	14.8, 17.0, 23.3	...	0.64, 0.79, 0.78	0.42 ± 0.3	1, 2
1420	1992 Feb 19	0348:47	..., 42.0, ...	...	..., 0.52, ...	0.23 ± 0.1	1
1534	1992 Apr 01	0050:19	11.2, 13.7, ...	...	0.52, 0.55, ...	...	
1668	1992 Jun 24	1853:16	..., 29.7, ...	29 ± 13	..., 0.93, ...	0.40 ± 0.1	1
1672	1992 Jun 25	1753:44	43.4, 38.5, 41.7	...	0.53, 0.55, 0.73	0.44 ± 0.3	1
1705	1992 Jul 17	2109:31	10.6, 9.8, ...	...	0.48, 0.51, ...	...	
1745	1992 Aug 05	2123:13	9.5, ..., ...	...	0.56, ..., ...	0.33 ± 0.2	1
1895	1992 Sep 05	1126:10	10.6, 11.1, ...	...	0.58, 0.58, ...	...	
1897	1992 Sep 06	0903:25	..., 12.5, ...	24 ± 7	..., 0.58, ...	0.50 ± 0.1	1
1898	1992 Sep 06	1151:03	..., 19.8, ...	...	..., 0.64, ...	...	
1923	1992 Sep 12	1538:36	25.2, 25.0, 24.6	...	0.69, 0.70, 0.91	...	
1933	1992 Sep 16	2349:21	14.9, 20.0, ...	...	0.76, 0.76, ...	...	
1977	1992 Oct 04	2217:06	..., 11.4, 15.0	22 ± 6	..., 0.53, 0.65	0.40 ± 0.1	1, 3
2009	1992 Oct 27	0145:17	14.6, 17.0, 17.1	...	0.56, 0.55, 0.43	...	
2178	1993 Feb 09	0719:10	13.6, 11.6, ...	24 ± 11	0.82, 0.76, ...	0.60 ± 0.1	1
2186	1993 Feb 11	1831:24	7.5, 8.5, ...	...	0.33, 0.51, ...	0.45 ± 0.3	1
2196	1993 Feb 17	1035:44	18.1, 19.3, 20.1	...	0.68, 0.69, 0.75	...	, 3
2200	1993 Feb 18	1056:48	25.4, 25.2, 26.3	...	0.65, 0.61, 0.54	0.39 ± 0.2	1
2299	1993 Apr 10	2119:23	6.4, ..., ...	...	0.56, ..., ...	0.41 ± 0.3	1
2543	1993 Sep 27	1207:21	..., 23.8, ...	...	..., 0.53, ...	0.45 ± 0.2	1
2559	1993 Oct 03	1242:33	28.0, ..., ...	74 ± 28	0.62, ..., ...	0.60 ± 0.1	1
2627	1993 Nov 12	1802:58	40.3, ..., ...	...	0.74, ..., ...	0.20 ± 0.1	1
2666	1993 Nov 30	0603:17	..., 38.1, ...	78 ± 11	..., 0.62, ...	0.30 ± 0.1	1, 4, 5
2779	1994 Jan 26	0539:54	13.4, 11.9, ...	25 ± 4	0.59, 0.65, ...	0.50 ± 0.1	1, 4, 5
3124	1994 Aug 14	1735:06	..., 15.4, ...	...	..., 0.71, ...	0.44 ± 0.3	1, 2

REFERENCES.—(1) Aschwanden, Dennis, & Schwartz 1998a; (2) Sakao, Kosugi, & Masuda 1998; (3) Masuda et al. 1994; (4) Nishio et al. 1997; (5) Bastian & Aschwanden 1999.

2.3. *Energy Dependence of Footpoint Distance*

Because a double footpoint structure is often visible in multiple HXT energy channels, we can test whether the footpoint distance, and thus the locations of electron precipitation sites, have any energy dependence. In Figure 4 (*left frame*) we show a scatter plot between the distances measured in the lowest energy channel (d_{Lo}) and the first medium channel (d_{M1}), which could be measured together in 29 flares. The average ratio between the two distances is $d_{M1}/d_{Lo} = 1.03 \pm 0.14$ and thus does not show any signifi-

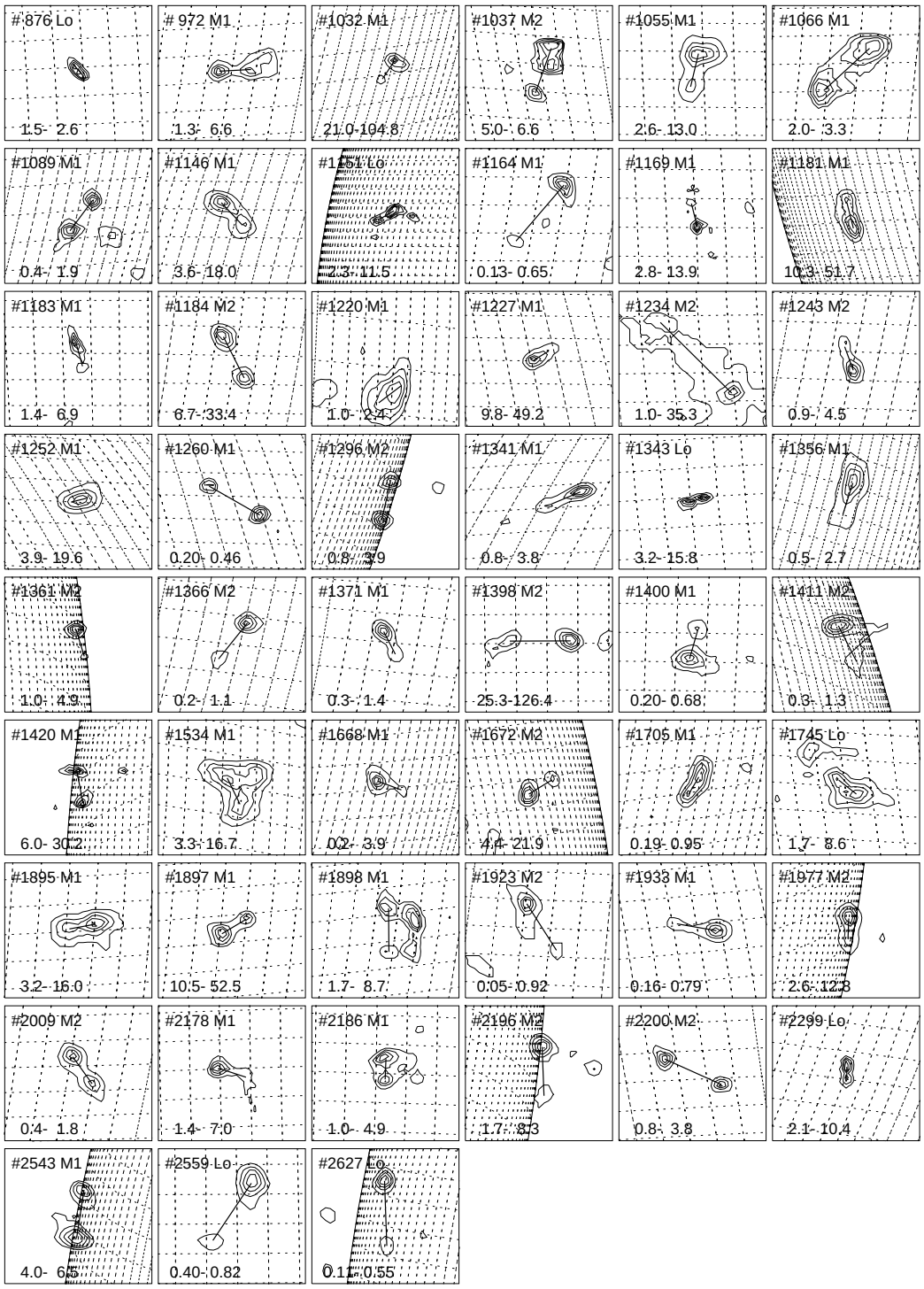

FIG. 1.—*Yohkoh*/HXT maps of analyzed 54 solar flares, labeled by the BATSE burst number (876, …, 3124) for which the observing dates, times, and measured parameters are listed in Table 1. From the three lower HXT energy channels (Lo = 14–23 keV, M1 = 23–33 keV, M2 = 33–53 keV) we show for each flare that HXT image with the highest energy in which the double footpoint structure was analyzable. The footpoint separation (defined by the distance between the two fitted Gaussian functions) is marked with a thick line. The contours of each HXT image are linearly spaced between a lower threshold $F_{\min}$ and the flux maximum $F_{\max}$ (typically 20%, 40%, 60%, 80%, 100%), with the range $[F_{\min}, F_{\max}]$ in counts s^{-1} per subcollimator indicated at the bottom of each frame. All frames have the same spatial scale of 32 HXT pixels in x- and y-axis (i.e., 78″.5 or 55,000 km). A heliographic coordinate system with a spacing of 1 heliographic degree (=12,150 km) is overlaid.

cant difference. In Figure 4 (*right frame*) we show how the distances of the two medium energy channels compare, having a ratio of $d_{M2}/d_{M1} = 1.05 \pm 0.16$ (for 14 flares), and thus do not deviate significantly from each other. The precipitation sites can therefore be considered as cospatial in the energy range of 14–53 keV.

2.4. *Energy Dependence of Footpoint Asymmetry*

In Figure 5 we show a comparison of the asymmetric flux ratios measured at different energies. The ratio of the flux asymmetries, $A_{M1}/A_{\rm Lo} = 1.12 \pm 0.26$, does not reveal a significant difference, although there is a larger number of

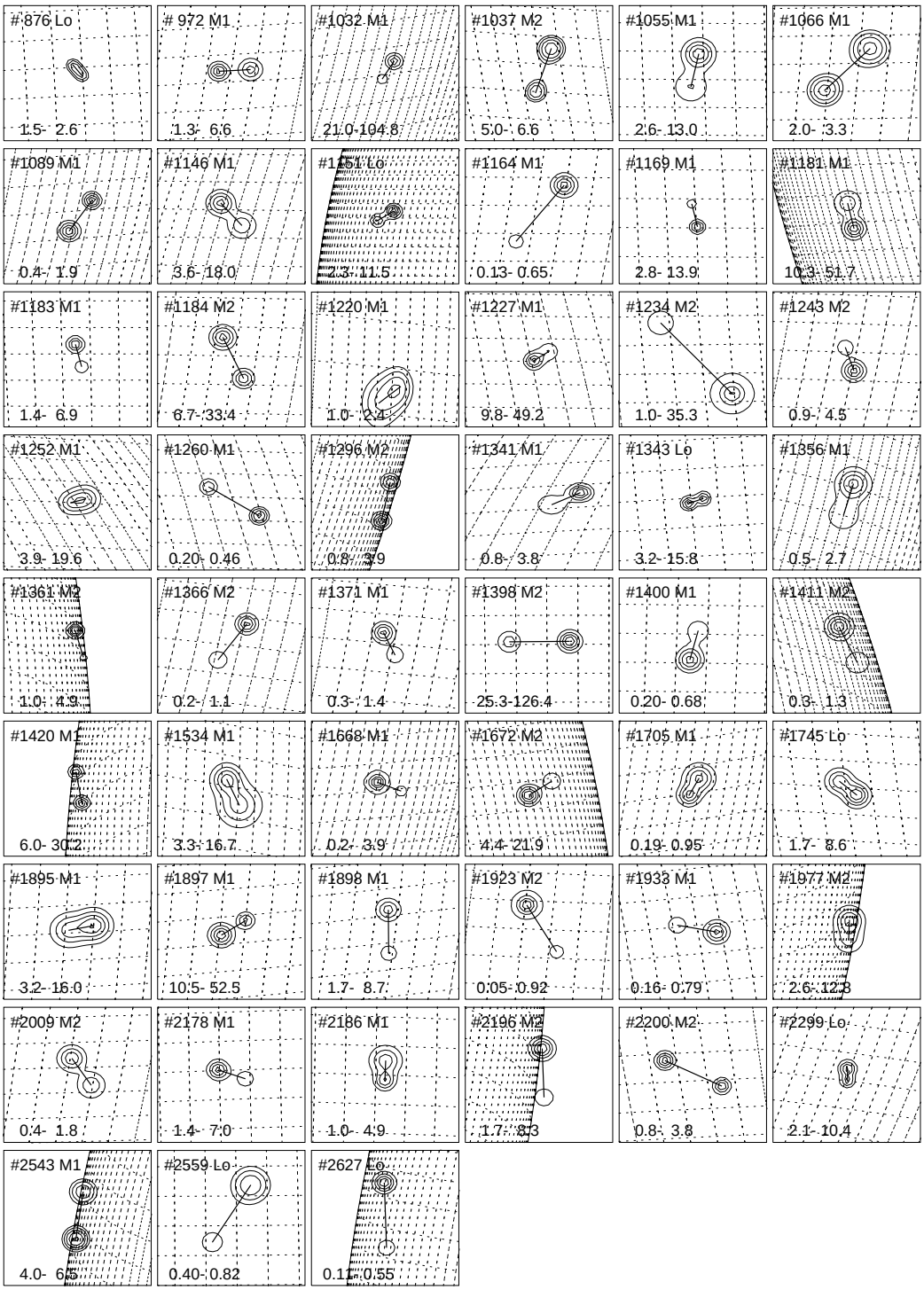

FIG. 2.—Fits of two-Gaussian component model to double footpoint sources of HXT maps shown in Fig. 1. The representation is identical to Fig. 1, with identical contour levels. The distance between the Gaussian centers defines the footpoint separation measurement. Note that the two-component model fits only the fluxes near the peaks of the footpoint sources, whereas no attempt was made to fit additional structures of the HXT map.

events that show less asymmetry in the Lo band than in the M1 band. This trend probably reflects the fact that the Lo band (14–23 keV) is more contaminated with thermal emission and nonthermal coronal energy loss, which tends to bridge the footpoints, and thus reduces the asymmetry of the footpoint fluxes to some extent. This confusion effect is clearly eliminated when we select only events with well-separated footpoints ($d > 20$ Mm), as shown for the subset marked with filled diamonds in Figure 5 (*left frame*), which has a tighter correlation of $A_{M1}/A_{\rm Lo} = 0.96 \pm 0.07$.

The ratio of the flux asymmetries in the higher channels, $A_{M2}/A_{M1} = 1.06 \pm 0.18$, is also close to unity (Fig. 5, *right frame*). This is plausible because these two energy channels (23–33 and 33–53 keV) are less contaminated by thermal HXR emission and thus should both measure the same nonthermal footpoint sources.

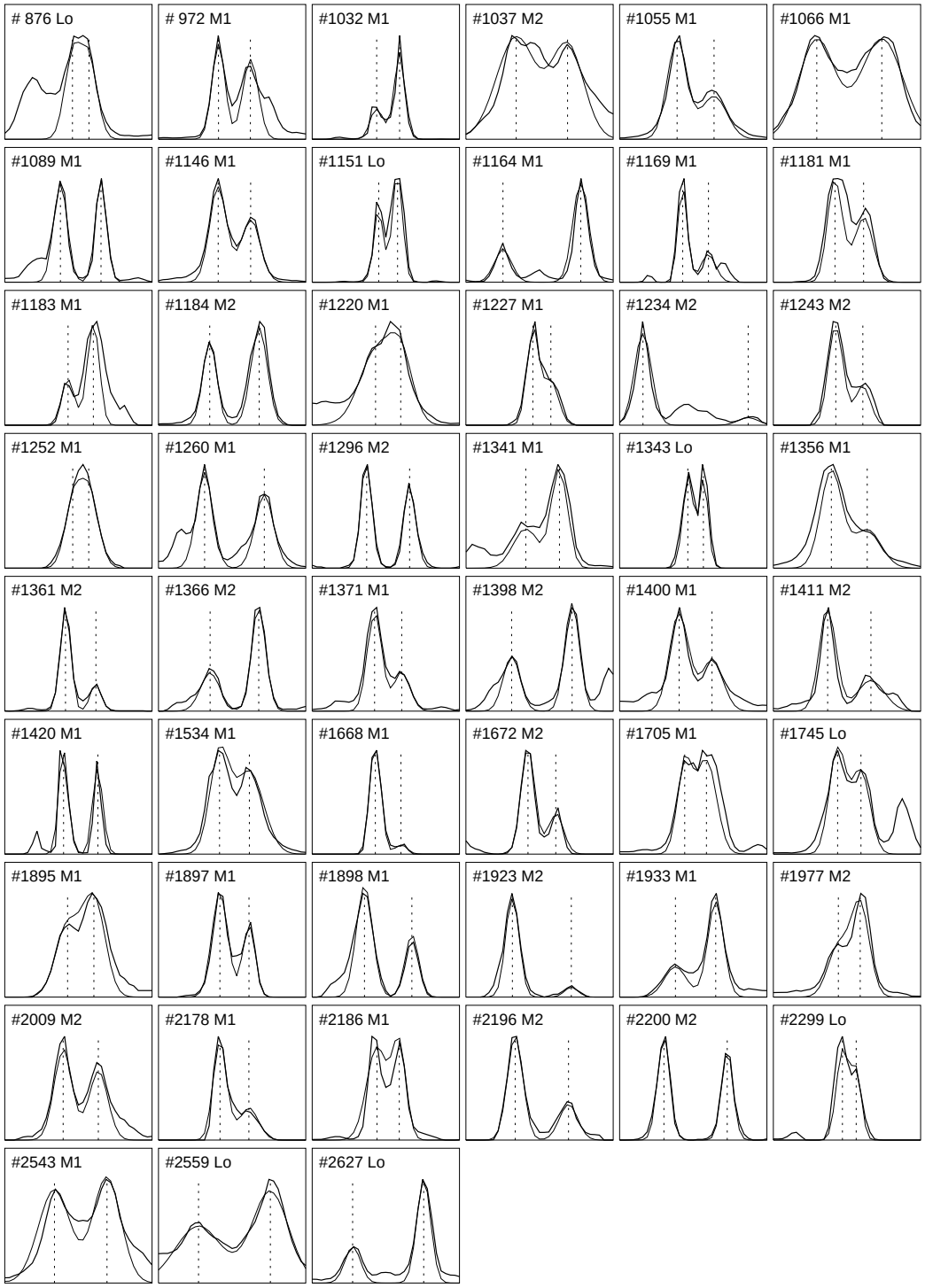

FIG. 3.—HXT flux profiles (bilinearly) interpolated along the footpoint baseline computed from the Gaussian fits as shown in Figs. 1 and 2. The observed flux is shown with a thick solid line (normalized), whereas the fit of the two-component Gaussian model is shown with a thin solid line (and the center positions of the Gaussians are marked with dashed lines). Note that the fits are optimized in the two-dimensional image plan and thus do not necessarily coincide with the best conceivable fit along a one-dimensional scan line, especially for source components that are not spherically symmetric.

2.5. *Energy Dependence of the Altitude of HXR Footpoints*

A lower limit on the altitude of HXR footpoint emission can only be inferred from the apparent height above the optical limb for HXR flares that occur very close to the limb. We find only one single flare from our set of 54 analyzed events that meets this criterion, i.e., flare 2196 of 1993 February 17, 1035:44 UT (see Fig. 1). For the southern HXR footpoint, which seems to have a heliographic position close to 90° west from the central meridian, based on the apparent altitude above the limb, we measure the following absolute altitude for the three lower HXR channels: $h_{\rm Lo} = 5900$ km, $h_{M1} = 4000$ km, and $h_{M2} = 3500$ km. Note that the altitudes decrease systematically with higher energies, but appear to be located slightly above the

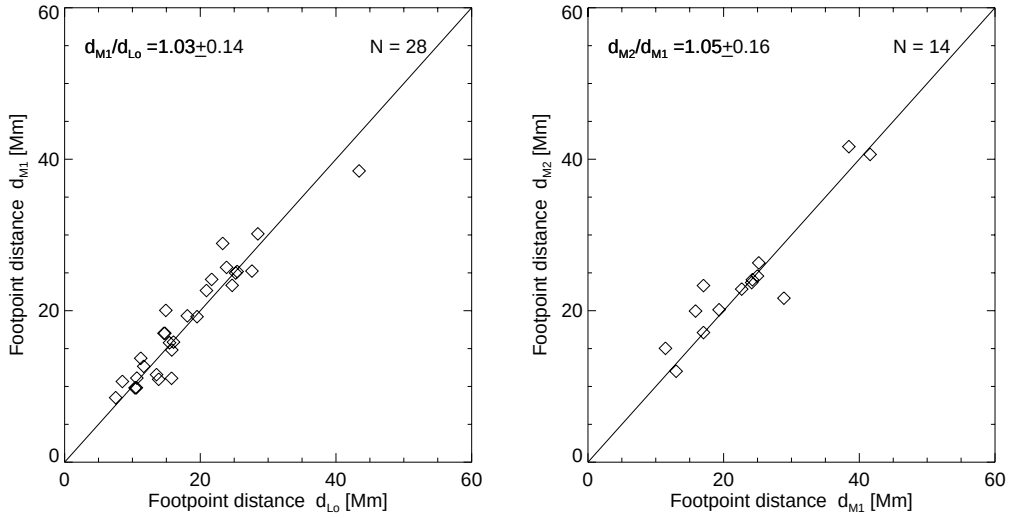

FIG. 4.—Scatter plot of footpoint distances measured at different energies: d_{M1} vs. $d_{\rm Lo}$ (*left frame*) and d_{M2} vs. d_{M1} (*right frame*). The mean and standard deviation of their ratios do not indicate a significant deviation from unity (*solid line*).

top of the chromosphere (which has a nominal height of 2500 km).

For all other flares we can only measure relative altitude differences between two energy channels by measuring their relative displacements and by correcting for projection effects. We measured these relative height differences for all footpoint sources with a flare position more than 45° from the central meridian and obtained the following statistical height differences (with a mean and standard error $\sigma/N^{1/2}$ of): $h_{\rm Lo} - h_{M1} = 980 \pm 250$ km and $h_{M1} - h_{M2} = 310 \pm 300$ km (see distributions in Fig. 6). The standard deviation σ of the measured altitude differences is $\sigma_{h_{\rm Lo}-h_{M1}} = 880$ km and $\sigma_{h_{M1}-h_{M2}} = 1100$ km, which is about a factor of 3–4 smaller than the nominal resolution of HXT ($\approx$3500 km). Again we note that the altitudes decrease systematically with higher energies.

3. MODELING AND DISCUSSION

We combine now the new parameters measured from *Yohkoh*/HXT (i.e., the footpoint distances d and asymmetry ratios A) with the previously analyzed HXR parameters measured from *CGRO* (i.e., the electron time-of-flight distance $l_{\rm TOF}$, the trap electron density n_e, and the precipitation ratios $q_{\rm prec}$; Aschwanden 1998 and Aschwanden, Dennis, & Schwartz 1998a, Papers I and II, respectively) in order to develop self-consistent physical models of the electron kinematics in flare loops.

3.1. *Scaling Law between Time-of-Flight Distance and HXR Footpoint Separation*

First we compare the spatial scales, i.e., the footpoint distance d measured with *Yohkoh*/HXT (Table 1) and the

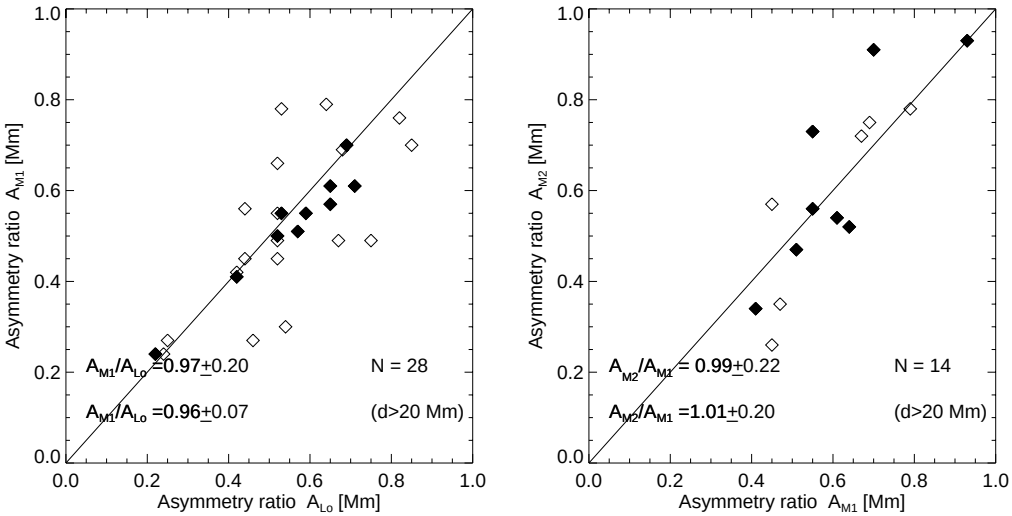

FIG. 5.—Comparison of footpoint asymmetries A measured at different energies: A_{M1} vs. $A_{\rm Lo}$ (*left frame*) and A_{M2} vs. A_{M1} (*right frame*). The mean and standard deviation of their ratios do not indicate a significant deviation from unity (*solid line*). Data points from flares with large footpoint separations ($d > 20$ Mm) are indicated with filled diamonds. These well-separated footpoints show a tighter correlation between the asymmetries $A_{\rm Lo}$ and A_{M1} because of less confusion by thermal emission that bridges the footpoints in the lowest energy channel (Lo).

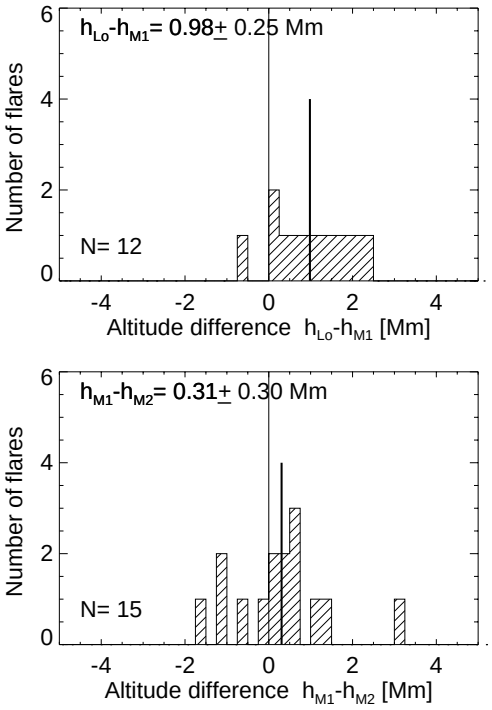

FIG. 6.—Distribution of altitude differences measured between the Lo and M1 channel (*top*) and between the M1 and M2 channel (*bottom*). The subset includes flares at longitudes $<45°$ near the limb. Note the trend of lower altitudes for higher energies.

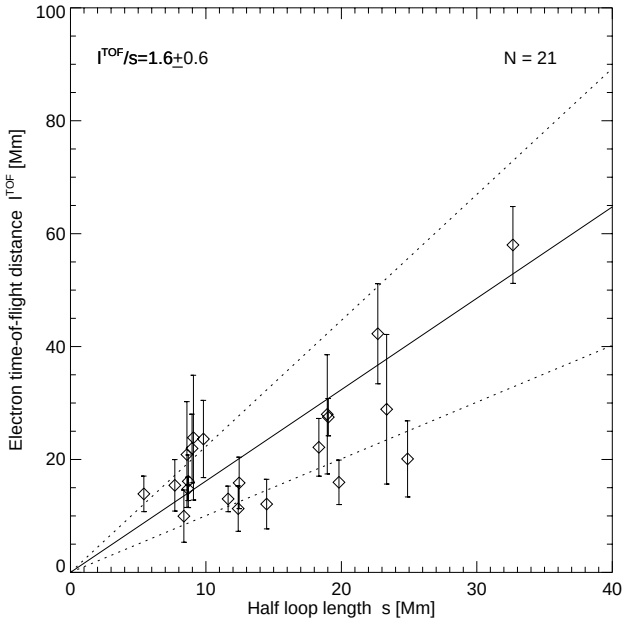

FIG. 7.—Scatter plot of flare loop half-length $s = (\pi/2)(d/2)$ measured with *Yohkoh*/HXT and electron time-of-flight distance $l_{\rm TOF}$ measured with *CGRO*. The vertical error bars indicate the uncertainty in the measurement of $l_{\rm TOF}$ due to the photon count statistics. The two spatial parameters show a correlation, with a mean (*solid line*) and standard deviation (*dotted line*) of $l_{\rm TOF}/s = 1.6 \pm 0.6$.

electron time-of-flight distance $l_{\rm TOF}$ measured from the energy-dependent time delays of the direct-precipitation electron component deconvolved from *CGRO* time profiles (Table 1 in Paper II). Note that the second spatial parameter, $l_{\rm TOF}$, is entirely determined from timing information without any spatial data. The two parameters could be measured jointly during simultaneous time intervals in 23 flares with reasonable accuracy (ignoring three flares with larger uncertainties of $\sigma_{\rm TOF} > 15$ Mm; see Table 1). In Figure 7 we display the electron time-of-flight distance $l_{\rm TOF}$ versus the loop half-length s, which is defined by $s = (\pi/2)(d/2)$ for a semicircular loop. The scatter plot shows a clear correlation, which can be expressed as a scaling law with a ratio of $l_{\rm TOF}/s = 1.6 \pm 0.6$. We recall that the time-of-flight distance derived here and in previous work includes mean correction factors for electron pitch angles ($q_\alpha = 0.64$) and the helicity of magnetic field lines ($q_H = 0.85$); see Appendices A and B in Aschwanden et al. (1996a).

This scaling law corroborates an earlier finding with a mean and standard deviation of $l_{\rm TOF}/s = 1.43 \pm 0.30$ (Fig. 5 in Aschwanden et al. 1996b) that has been discovered from the same data but with less refined analysis methods. The electron time-of-flight distance has been measured in this earlier work by Fourier-filtering of the pulsed HXR flux, whereas the filtering of the direct-precipitation from the trap-precipitation component has been accomplished here with a deconvolution method based on a physical model. The fact that the new ($l_{\rm TOF}/s = 1.6 \pm 0.6$) and the old result ($l_{\rm TOF}/s = 1.4 \pm 0.3$) are found to be consistent speaks for the robustness of both methods. In particular we would like to emphasize that $l_{\rm TOF}/s \gtrsim 1.0$ represents a lower limit in both methods.

The essence of this lower limit in both results is that electrons appear to be accelerated *above* the loop top rather than at the loop top, consistent with the location of Masuda's *above-the-loop top* sources (Masuda et al. 1994), which are presumably attributable to the acceleration site itself. Alternatively, in flares that do exhibit a more complex topology than a single loop with a cusp structure, e.g., multiply interacting loops as presented by Hanaoka (1997) or Nishio et al. (1997), our scaling law indicates that the acceleration site is also located slightly above the primary compact HXR flare loop, perhaps near the interaction point with an overarching larger secondary flare loop.

3.2. *Asymmetric Trap Model*

The timing analysis of *CGRO* data, based on the total HXR flux without spatial information, provides a global electron trapping timescale. The spatial structure, however, can often be described by two magnetically conjugate footpoint sources, which often have asymmetric HXR fluxes according to the *Yohkoh*/HXT images. These unequal double footpoint sources indicate electron precipitation sites in a flare loop with asymmetric magnetic field geometry. We need therefore to develop an asymmetric trap model to relate the trapping time information from *CGRO* data to the asymmetric double footpoint sources seen in *Yohkoh* HXT data.

In order to mimic an asymmetric trap model we rotate the reference system of a symmetric dipole-like magnetic field by an angle ψ, as shown with three examples in Figure 8 (*top*): the symmetric case with $\psi = 0$ (*left*), a weakly asymmetric case where the dipole coil is rotated by $\psi = 30°$ (*middle*), and strongly asymmetric case where the coil is rotated by $\psi = 60°$. (A spherically symmetric sunspot with a "monopolar" vertical field would correspond to the extreme case of $\psi = 90°$.) The acceleration or injection site into the trap is assumed to be midway (with a magnetic field

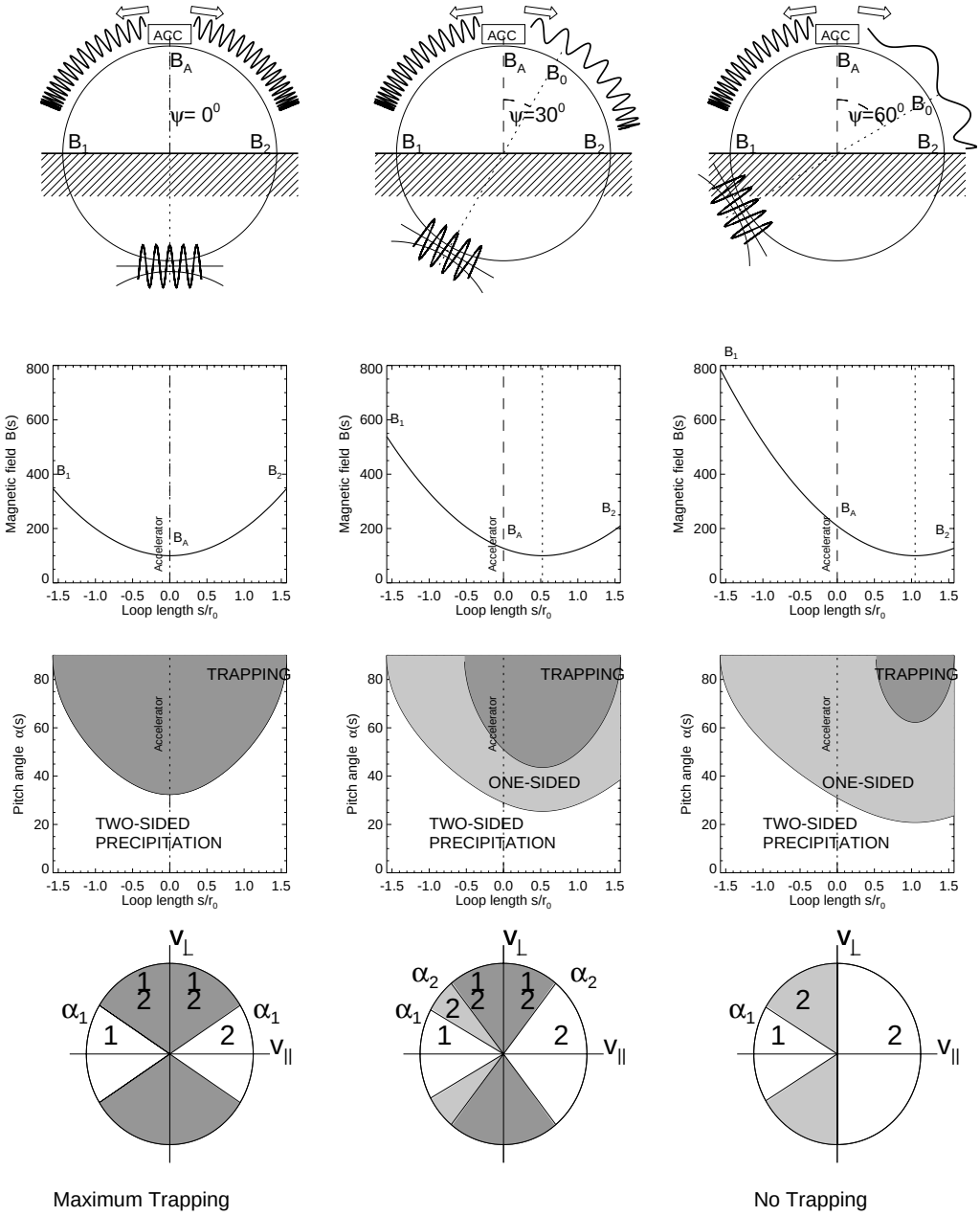

FIG. 8.—Three model scenarios for a symmetric (*left column*), a slightly asymmetric (*middle column*), and strongly asymmetric magnetic trap (*right column*). The spatial configuration of a buried dipole and the resulting pitch-angle motion of trapped and/or precipitating electrons is sketched (*top row*); the magnetic field $B(s)$ is parametrized as function of the loop coordinate s (*second row*); the pitch-angle variation $\alpha(s)$ as function of the loop coordinate and three pitch-angle regimes are shown (*third row*); and the corresponding pitch-angle regimes in velocity space ($v_{\|}$, $v_{\perp}$) are shown (*bottom row*). The numbers 1 and 2 correspond to the left and right loss-cone site, with the stronger magnetic field located at footpoint 1 (see explanations in § 2.3).

B_A) between the two footpoints (with magnetic fields B_1 and B_2). These three magnetic field values B_A, B_1, B_2 are decisive concerning what fraction of electrons are trapped or precipitate to the two footpoints. Because of conservation of the magnetic moment, $\mu = \frac{1}{2} m_e v_{\perp}^2 / B \propto \sin \alpha(s)^2 / B(s) =$ const, the critical pitch angles that separate precipitating from trapped particles at the two footpoints are defined by the *magnetic mirror ratios*

$$R_1 = \frac{B_1}{B_A} = \frac{1}{\sin (\alpha_1)^2} , \tag{4}$$

$$R_2 = \frac{B_2}{B_A} = \frac{1}{\sin (\alpha_2)^2} . \tag{5}$$

For positive rotation angles $\psi > 0$ the magnetic field at footpoint B_1 is stronger ($B_1 > B_2$, $R_1 > R_2$), and the critical angle, also called *loss-cone angle*, is smaller ($\alpha_1 < \alpha_2$) than at the opposite footpoint 2. The asymmetric magnetic field $B(s)$ along a flare loop is visualized in Figure 8 (*second row*) with a quadratic model. Note that in the case with strong asymmetry ($\psi = 60^{\circ}$), trapping is not possible because $B_2 < B_A$, corresponding to a mirror ratio $R_2 < 1$.

The pitch-angle variation $\alpha(s)$ along the loop according to conservation of the magnetic moment is shown in Figure 8 (*third row*). Generally, three regimes can be distinguished in the α-s plane: (1) a direct-precipitation regime for initial pitch angles $0 < \alpha(s = 0) < \alpha_1$, (2) a secondary precipitation regime after one mirror bouncing for initial pitch angles

$\alpha_1 < \alpha(s = 0) < \alpha_2$, and (3) a trapping regime for initial pitch angles $\alpha_2 < \alpha(s = 0) < \pi/2$. These three regimes are clearly discernible in the case with weak asymmetry ($\psi = 30°$, Fig. 8, *middle column*). For the symmetric case, the secondary precipitation regime collapses to zero because $\alpha_1 = \alpha_2$ (Fig. 8, *left column*). For the strongly asymmetric case ($\psi = 60°$) no trapping is possible because there is no solution for $\alpha_2 < \pi/2$ with $R_2 < 1$ (see eq. [5]).

After we have a quantitative description of the pitch-angle ranges that contribute to trapping and precipitation at both footpoints, we can now calculate the relative fractions of precipitating electrons at the two footpoints and obtain quantitative expressions for the HXR flux asymmetry A. We visualize the pitch-angle regimes in velocity space ($v_\parallel$, $v_\perp$) (in Fig. 8, *bottom*) and label the different regimes with the footpoint numbers 1 and 2, to which the electrons precipitate, either directly, after one mirror bounce, or after intermediate trapping. We determine now the relative fractions of precipitating electrons by integration over the corresponding pitch-angle ranges in velocity space. Here and in the following we assume an isotropic pitch-angle distribution at the acceleration/injection site [$f(\alpha) = \text{const}$]. The fraction $q_{\rm DP1}$ of directly precipitating electrons at footpoint 1, which has the smaller loss cone ($\alpha_1 \leq \alpha_2$), is

$$q_{P1} = q_{\rm DP1} = \frac{\int_{\pi-\alpha_1}^{\pi} f(\alpha) \sin(\alpha)\, d\alpha}{\int_0^{\pi} f(\alpha) \sin(\alpha)\, d\alpha} = \frac{(1 - \cos\alpha_1)}{2} . \quad (6)$$

The fraction of directly precipitating electrons at footpoint 2, which has the larger loss-cone angle (α_2), includes not only those electrons that precipitate without bouncing ($q_{\rm DP2}$) but also those that bounce once at the mirror site 1 ($q_{\rm MP2}$) and precipitate then at footpoint 2, i.e., with initial pitch angles of $(\pi - \alpha_2) < \alpha(s = 0) < (\pi - \alpha_1)$,

$$\begin{aligned} q_{P2} &= q_{\rm DP2} + q_{\rm MP2} \\ &= \frac{\int_0^{\alpha_2} f(\alpha) \sin(\alpha)\, d\alpha + \int_{\pi-\alpha_1}^{\pi-\alpha_2} f(\alpha) \sin(\alpha)\, d\alpha}{\int_0^{\pi} f(\alpha) \sin(\alpha)\, d\alpha} \\ &= \frac{(1 + \cos\alpha_1 - 2\cos\alpha_2)}{2} . \end{aligned} \quad (7)$$

From the spatially unresolved *CGRO* data we measured the combined fraction $q_{\rm prec}$ of directly precipitating electrons at both footpoints, which is equivalent to the sum of both footpoint components q_{P1} and q_{P2},

$$q_{\rm prec} = q_{P1} + q_{P2} = 1 - \cos\alpha_2 . \quad (8)$$

The total fraction of trapped electrons is determined by the pitch-angle range of the larger loss cone, i.e., $\alpha_2 < \alpha(s = 0) < (\pi - \alpha_2)$,

$$q_T = \frac{\int_{\alpha_2}^{\pi-\alpha_2} f(\alpha) \sin(\alpha)\, d\alpha}{\int_0^{\pi} f(\alpha) \sin(\alpha)\, d\alpha} = \cos\alpha_2 = (1 - q_{\rm prec}) . \quad (9)$$

Trapped electrons are randomly scattered, but their pitch angle increases statistically with time, until they diffuse into a loss cone. Because collisional deflection is an accumulative process of many small-angle scattering deflections that can add up to a small or large net value after each loop transit, there is some probability that trapped electrons can escape on either loss-cone side. The escape probability on the side with the larger loss cone is higher than at the opposite side with the smaller loss cone. In first order we estimate that the relative escape probabilities from the trap toward the two loss-cone sides be proportional to the probabilities for direct precipitation at the two loss-cone sides (for particles with pitch angles $\alpha \leq \alpha_2$),

$$q_{T1} = q_T \left(\frac{q_{P1}}{q_{\rm prec}} \right) , \quad (10)$$

$$q_{T2} = q_T \left(\frac{q_{P2}}{q_{\rm prec}} \right) . \quad (11)$$

The proportionality implies also symmetric escape probabilities for symmetric loss cones. We emphasize that this proportionality *Ansatz* $q_{T1}/q_{T2} \approx q_{P1}/q_{P2}$ represents an approximation we employ for mathematical convenience. A more rigorous treatment of the asymmetric escape probabilities can be derived with statistical theory or with numerical simulations. Numerical simulations using the Fokker-Planck equation are presented in a separate study (Fletcher & Aschwanden 1999). In these numerical simulations we find that the proportionality assumption represents a reasonable approximation.

To estimate the relative HXR fluxes at both footpoints, we have to sum the precipitating and trapped contributions at both sides. We denote the combined fractions at both footpoints by q_1 and q_2,

$$q_1 = q_{P1} + q_{T1} = q_{P1} \left(1 + \frac{q_T}{q_{\rm prec}} \right) = q_{P1} \left(\frac{1}{q_{\rm prec}} \right) , \quad (12)$$

$$q_2 = q_{P2} + q_{T2} = q_{P2} \left(1 + \frac{q_T}{q_{\rm prec}} \right) = q_{P2} \left(\frac{1}{q_{\rm prec}} \right) . \quad (13)$$

Neglecting differences in the spectral slope (e.g., arising from asymmetric accelerators or asymmetric coronal energy loss), the HXR flux at a given energy ε is proportional to the number of (nonthermal) electrons with energies $E \gtrsim \varepsilon$. Assuming a similar spectral slope of the electron injection spectrum toward the two opposite directions 1 and 2, the HXR fluences $F_1 = \int f_1(t)dt$ and $F_2 = \int f_2(t)dt$ observed at the two footpoints are then expected to be proportional to the precipitating electron fluxes q_1 and q_2. This constitutes a relation between the observed HXR flux asymmetry A and the loss-cone angle α_2,

$$A = \frac{F_2}{(F_1 + F_2)} = \frac{q_2}{(q_1 + q_2)} = q_2 = (1 - q_1) . \quad (14)$$

With these relations (eqs. [6], [8], [12], [14]) we have a simple method to determine the two loss-cone angles α_1 and α_2 from the observables $q_{\rm prec}$ and A,

$$\alpha_1 = \arccos\left[1 - 2(1 - A) q_{\rm prec}\right] , \quad (15)$$

$$\alpha_2 = \arccos\left(1 - q_{\rm prec}\right) , \quad (16)$$

and the corresponding magnetic mirror ratios R_1 and R_2 with equations (4) and (5), or the ratios of the magnetic fields B_1/B_A and B_2/B_A, respectively.

3.3. *Observed Loss-Cone Angles and Magnetic Mirror Ratios*

Based on the measurements of the HXR flux asymmetries A from *Yohkoh*/HXT data (Table 1) and the precipitation ratios $q_{\rm prec}$ from *CGRO* (Paper II) we calculated the loss-cone angles α_1 and α_2 with equations (15) and (16) using the

TABLE 2

PHYSICAL PARAMETERS OF ELECTRON PRECIPITATION AND TRAPPING IN 44 FLARES

BATSE Number	HXT Channel	Direct Precipitation		Trap Precipitation	Loss-Cone Angles	Magnetic Mirror Ratios	Magnetic Field Ratio
		q_{P1}	q_{P2}	$(q_T = q_{T1} + q_{T2})$	(α_1, α_2)	(R_1, R_2)	(B_1/B_2)
876.....	Lo	0.17	0.18	0.65	49, 49	1.75, 1.73	1.01
972.....	M1	0.18	0.22	0.60	49, 53	1.72, 1.56	1.10
1032.....	M1	0.05	0.15	0.80	26, 36	4.89, 2.78	1.76
1037.....	M2	0.14	0.16	0.70	44, 45	2.03, 1.96	1.04
1055.....	M1	0.18	0.42	0.40	50, 66	1.69, 1.19	1.42
1066.....	M1	0.25	0.25	0.50	59, 60	1.34, 1.33	1.00
1089.....	M1	0.25	0.26	0.49	59, 60	1.34, 1.32	1.02
1146.....	M1	0.16	0.24	0.60	46, 53	1.89, 1.56	1.21
1151.....	Lo	0.19	0.31	0.50	52, 60	1.60, 1.33	1.20
1164.....	M1	0.11	0.34	0.55	38, 56	2.59, 1.43	1.81
1169.....	M1	0.09	0.31	0.60	34, 53	3.07, 1.56	1.96
1181.....	M1	0.23	0.37	0.40	56, 66	1.43, 1.19	1.20
1183.....	M1	0.06	0.14	0.80	28, 36	4.48, 2.78	1.61
1184.....	M2	0.05	0.05	0.90	25, 25	5.57, 5.26	1.06
1220.....	M1	0.09	0.11	0.80	35, 36	2.91, 2.78	1.05
1227.....	M1	0.15	0.32	0.53	45, 57	1.99, 1.39	1.43
1234.....	M2	0.04	0.56	0.40	24, 66	5.85, 1.19	4.91
1243.....	M2	0.12	0.30	0.58	40, 54	2.38, 1.51	1.58
1296.....	M2	0.13	0.17	0.70	42, 45	2.16, 1.96	1.10
1341.....	M1	0.08	0.22	0.70	32, 45	3.38, 1.96	1.72
1343.....	Lo	0.19	0.21	0.60	51, 53	1.62, 1.56	1.04
1356.....	M1	0.15	0.39	0.46	46, 62	1.93, 1.27	1.52
1361.....	M2	0.06	0.26	0.68	28, 47	4.35, 1.86	2.34
1366.....	M2	0.10	0.30	0.60	37, 53	2.69, 1.56	1.72
1371.....	M1	0.12	0.30	0.58	39, 54	2.45, 1.51	1.63
1398.....	M2	0.07	0.13	0.80	30, 36	3.96, 2.78	1.43
1400.....	M1	0.07	0.13	0.80	30, 36	3.94, 2.78	1.42
1411.....	M2	0.09	0.33	0.58	35, 54	2.94, 1.51	1.95
1420.....	M1	0.11	0.12	0.77	38, 39	2.56, 2.46	1.04
1668.....	M1	0.03	0.37	0.60	19, 53	9.01, 1.56	5.76
1672.....	M2	0.12	0.32	0.56	40, 55	2.40, 1.46	1.65
1745.....	Lo	0.15	0.18	0.67	44, 47	2.01, 1.81	1.11
1897.....	M1	0.21	0.29	0.50	54, 60	1.51, 1.33	1.13
1977.....	M2	0.14	0.26	0.60	44, 53	2.06, 1.56	1.32
2178.....	M1	0.14	0.46	0.40	44, 66	2.03, 1.19	1.70
2186.....	M1	0.22	0.23	0.55	56, 56	1.45, 1.43	1.01
2200.....	M2	0.18	0.21	0.61	49, 52	1.70, 1.59	1.07
2299.....	Lo	0.18	0.23	0.59	50, 53	1.68, 1.53	1.09
2543.....	M1	0.21	0.24	0.55	54, 56	1.51, 1.43	1.05
2559.....	Lo	0.23	0.37	0.40	57, 66	1.41, 1.19	1.19
2627.....	Lo	0.05	0.15	0.80	26, 36	5.08, 2.78	1.83
2666.....	M1	0.12	0.18	0.70	39, 45	2.45, 1.96	1.25
2779.....	M1	0.17	0.33	0.50	49, 60	1.73, 1.33	1.30
3124.....	M1	0.13	0.31	0.56	41, 55	2.25, 1.46	1.54

asymmetric trap model described in the previous section (§ 3.2). The resulting loss-cone angles for both footpoints are tabulated in Table 2 and their distribution is shown in Figure 9 (*middle panel*). The loss-cone angles on the side with the stronger magnetic field have a mean and standard deviation of $\alpha_1 = 42^\circ \pm 11^\circ$, whereas those on the side with the weaker magnetic field have $\alpha_2 = 52^\circ \pm 10^\circ$.

The fractions of directly precipitating electrons have a mean of $q_{P1} = 0.14 \pm 0.06$ at footpoint 1 and $q_{P2} = 0.26 \pm 0.10$ at footpoint 2, whereas the mean fraction of trapped electrons is $q_T = 0.60 \pm 0.13$. Their distributions are shown in Figure 9 (*top frame*).

The computation of loss-cone angles constrains the magnetic mirror ratios in our model (eqs. [4], [5]). The values are tabulated in Table 2 and their distribution is shown in Figure 9 (*bottom frame*). The magnetic mirror ratio between the footpoint with the stronger magnetic field and the acceleration/injection site at the loop top is found to have a median value of $R_1 = B_1/B_A = 2.1$ (with a 67% median range of $R_1 = 1.6, \ldots, 4.0$) for the flares analyzed here. The magnetic mirror ratio between the footpoint with the weaker magnetic field and the acceleration/injection site has a median value of $R_2 = B_2/B_A = 1.6$ (with a 67% median range of $R_1 = 1.3, \ldots, 2.5$). The ratio R_1/R_2 permits a prediction of the magnetic field ratio between the two footpoints B_1/B_2. This ratio of the magnetic fields at the footpoints is found to have a median value of $B_1/B_2 = 1.2$ (with a 67% median range of $B_1/B_2 = 1.1, \ldots, 1.8$). It will be interesting to compare these magnetic field ratios, which are predicted solely on the basis of observed HXR flux asymmetries, with the photospheric magnetic field strengths as they can be measured from magnetograms.

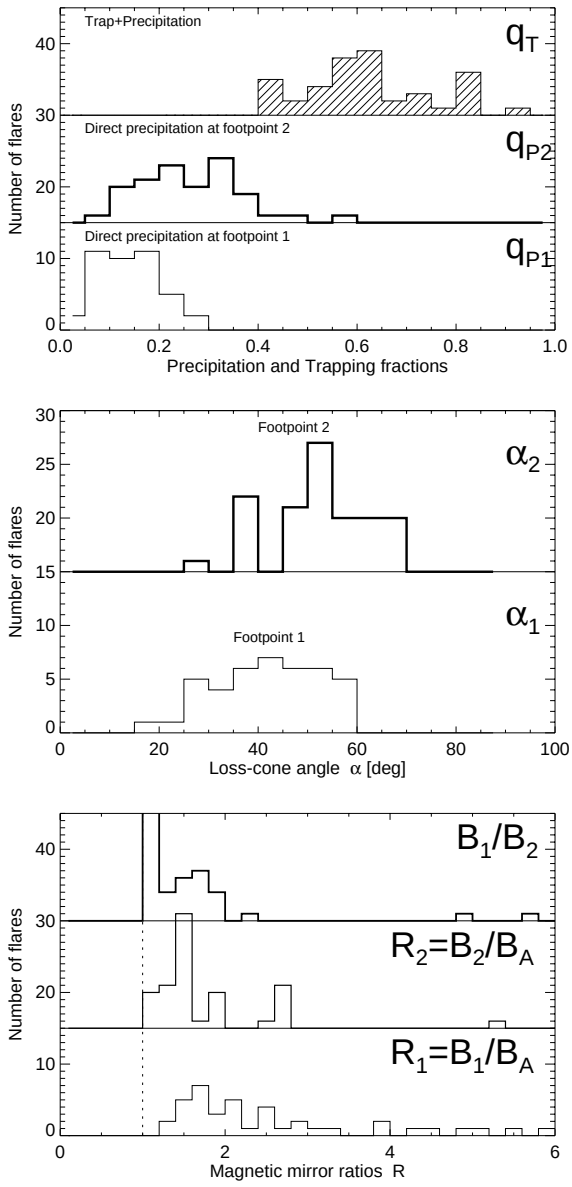

FIG. 9.—Distributions of precipitation and trapping fractions (*top*), conjugate loss-cone angles (*middle*), and magnetic mirror ratios (*bottom*), calculated for an isotropic pitch-angle distribution at the acceleration/injection site (see numerical values in Table 2).

3.4. *Stopping Depth and Thick-Target Density*

The altitude dependence for HXR emission sites found in § 2.5 is consistent with the thick-target model. From the altitudes measured in the 1993 February 17 flare we can determine the density and scale height of the thick target. The stopping depth (including scattering) is according to Brown (1972)

$$N_s = \mu_0 \frac{E_0^2}{3K} \approx 0.92 \times 10^{17} E_{\rm keV}^2 \ ({\rm cm}^{-2}) \,, \qquad (17)$$

with E_0 the initial electron energy, μ_0 the initial pitch angle, and the constant $K = 2\pi e^4 \Lambda \approx 9.3 \times 10^{-36}$ (cgs units). For the characteristic electron energies $E_i \approx 1.1\varepsilon_i$ we find for the lowest three HXT channels ($\varepsilon_1 = 14$ keV, $\varepsilon_2 = 23$ keV, and $\varepsilon_3 = 33$ keV) the following stopping depths: $N_s = (2.2, 5.9, 12.1) \times 10^{19}$ cm^{-2}. Using an exponential density model for the stopping depth,

$$N_s = \int_{-\infty}^{h_s} n_p(h')\, dh' = \int_{-\infty}^{h_s} n_{p,0} \exp\left(-\frac{h}{\lambda}\right) dz'$$

$$= n_{p,0}\, \lambda \exp\left(-\frac{h_s}{\lambda}\right), \qquad (18)$$

and the observed heights $h_s = 5900$, 4000, and 3500 km, we find that a base density of $n_{p0} = 2.6 \times 10^{12}$ cm^{-3} and a scale height of $\lambda = 1900$ km reproduce the stopping depths inferred from equation (17). The inferred thick-target densities at the three stopping heights are then $n_p(h_s) = (1.1, 3.1, 4.1) \times 10^{11}$ cm^{-3}. Note that Matsushita et al. (1992) found somewhat larger mean altitudes ($h_2 =$ 9700,8700,7700 km) for the same three HXT energy channels.

4. CONCLUSIONS

We measured the footpoint distance d and flux asymmetry A in 54 *Yohkoh*/HXT double footpoint flares, a data set that includes all flare events for which also the electron time-of-flight distance $l_{\rm TOF}$, the ambient electron density n_e in the trap, and the fraction $q_{\rm prec}$ of directly precipitating (or the trapping efficiency $1 - q_{\rm prec}$) has been measured from *CGRO* data (in Paper II). Although the nonimaging data from *CGRO* allow us only to distinguish two electron components, i.e., directly precipitating and trap-precipitating electrons, the imaging data from *Yohkoh*/HXT permit us furthermore to break down these two basic components at both footpoints separately, leading to four components (P1, P2, T1, T2), which are modeled in this study with an asymmetric trap model. The major findings of this analysis are

1. The *separation distance d* of conjugate HXR footpoints was measured in a range of $d = 8$–42 Mm, with a median value of $d_{\rm median} = 19$ Mm in the M1 channel. We did not found a significant difference in the footpoint distances between the Lo, M1, and M2 energy channel. The electron precipitation site can therefore be considered to be cospatial in the 14–53 keV energy range. The footpoint separation is also found to correlate with the electron time-of-flight distance, yielding a scaling law of $l_{\rm TOF}/s = 1.6 \pm 0.6$ with the half-loop length s. This result is consistent with an earlier finding (Aschwanden et al. 1996b) and suggests the electron acceleration site to be located *above* the apex of the HXR loop top.

2. The *altitude h* of HXR footpoint emission could be determined directly in one flare located very close to the limb. The altitudes are found to decrease systematically with higher energies: $h_{\rm Lo} = 5900$ km, $h_{M1} = 4000$ km, $h_{M2} = 3500$ km. For most of the other flares we could measure the relative altitude difference and find the same statistical trend: $h_{\rm Lo} - h_{M1} = 980 \pm 250$ km and $h_{M1} - h_{M2} = 310 \pm 300$ km. This trend is consistent with the expected energy loss site in a thick-target model with a density gradient (decreasing with height), e.g., as modeled in Fletcher (1996). The trend of decreasing altitudes with higher energies is also consistent with the previous result of Matsushita et al. (1992), based on correlations between HXT and Hα flare positions.

3. The *asymmetry A* of the HXR flux in resolved double footpoint sources ranges from fully symmetric $A = f_2/(f_1 + f_2) = 0.5$ to highly asymmetric values $A \leq 0.93$. No sig-

nificant energy dependence of this flux asymmetry is found statistically. We find that the asymmetry is inversely correlated with the trapping efficiency. Symmetric traps account for the highest trapping efficiency.

4. An *asymmetric trap model* is required to interpret the observed HXR flux asymmetry. Assuming (1) an isotropic pitch-angle distribution at the acceleration/injection site near the loop top and (2) double-sided trap precipitation with escape probabilities that are proportional to the direct-precipitation rates, i.e., $q_{T1}/q_{T2} = q_{P1}/q_{P2}$, we determine the relative fractions of both direct- and trap-precipitation components at the two footpoints, which have the following mean values: $q_{P1} = 0.14 \pm 0.06$, $q_{P2} = 0.26 \pm 0.10$, and $q_T = q_{T1} + q_{T2} = 0.60 \pm 0.13$. The model with double-sided trap precipitation, which predicts no relative time delay between conjugate HXR emission, is consistent with Sakao's (1994) simultaneity measurements of conjugate HXR sources.

5. The *loss-cone angles* α inferred from the asymmetric trap model under the assumption of isotropic injection were found to have mean values of $\alpha_1 = 42^\circ \pm 11^\circ$ at the side with the stronger magnetic field and $\alpha_2 = 52^\circ \pm 10^\circ$ at the side with the weaker magnetic field.

6. The *magnetic mirror ratios* R deduced with the asymmetric trap model were found to have median values of $R_1 = B_1/B_A = 2.1$ at the side with the stronger magnetic field, and $R_2 = B_2/B_A = 1.6$ at the side with the weaker magnetic field. The statistical ratio of the magnetic fields at the footpoints is predicted to have a median value of $R_1/R_2 = 1.2$.

This work has shown that timing studies (using a deconvolution technique to separate undelayed from trap-delayed electron components) in conjunction with measurements of the spatial asymmetry of magnetically conjugate HXR footpoint sources provides important information to estimate the coronal magnetic field in a flare loop and to constrain the resulting particle kinematics. In particular we obtained a simple *asymmetric trap model* that quantifies the relative fractions of directly and trapped precipitating electrons at both footpoints. This information is a necessary ingredient to model and understand the resulting photon bremsstrahlung spectrum at both footpoints, which has been modeled in previous work largely without considering the consequences of asymmetric magnetic field geometries, which seem to govern most of the flares. The information on asymmetric traps is even more important for modeling of (HXR correlated) gyrosynchrotron emission in radio wavelengths (e.g., see Gary 1985; Gary & Tang 1985; Bastian, Benz, & Gary 1998), an emission that is largely produced by trapped electrons and is extremely sensitive to the electron pitch angle. A model computation of a radio map involving gyrosynchrotron emission requires therefore a realistic spatial model of the (asymmetric) coronal magnetic field. Combining the magnetic field ratios of conjugate footpoints (predicted by asymmetric trap models here) with the actually observed magnetic field ratios at the photospheric footpoints may also provide constraints on the initial pitch-angle distribution of acceleration particles.

We would like to thank David Alexander and the anonymous referee for helpful comments to improve the paper. This work was supported by NASA *Yohkoh*/SXT contract NAS8-40108. The HXR data used in this paper are taken by the *Yohkoh* mission of ISAS, Japan, which was prepared and is operated by the international collaboration of Japanese, US, and UK scientists under the support of ISAS, NASA, and SERC, respectively.

REFERENCES

Aschwanden, M. J. 1998, ApJ, 502, 455 (Paper I)
Aschwanden, M. J., Dennis, B. R., & Schwartz, R. A. 1998a, ApJ, 502, 468 (Paper II)
Aschwanden, M. J., Hudson, H. S., Kosugi, T., & Schwartz, R. A. 1996a, ApJ, 464, 985
Aschwanden, M. J., Kosugi, T., Hudson, H. S., Wills, M. J., & Schwartz, R. A. 1996b, ApJ, 470, 1198
Aschwanden, M. J., Newmark, J., Delaboudiniére, J.-P., Neupert, W., Klimchuk, J. A., Gary, G. A., Portier-Fozzani, F., & Zucker, A. 1999, ApJ, in press
Aschwanden, M. J., Wills, M. J., Hudson, H. S., Kosugi, T., & Schwartz, R. A. 1996c, ApJ, 468, 398
Bastian, T. S., Benz, A. O., & Gary, D. E. 1988, ARA&A, 36, 131
Bastian, T. S., & Aschwanden, M. J. 1999, in preparation
Brown, J. C. 1972, Solar Phys., 26, 441
Duijveman, A., Hoyng, P., & Machado, M. E. 1982, Sol. Phys., 81, 137
Fletcher, L. 1996, A&A, 310, 661
Fletcher, L., & Aschwanden, M. J. 1999, in preparation
Gary, D. E. 1985, ApJ, 297, 799
Gary, D. E., & Tang, F. 1985, ApJ, 288, 385
Hanaoka, Y. 1997, Sol. Phys., 173, 319
Kosugi, T., et al. 1991, Sol. Phys., 136, 17
Kosugi, T., & *Yohkoh* HXT Group. 1993, The *Yohkoh* HXT Databook (I), 1991 October–1992 December, Natl. Astron. Obs., Mitaka, Tokyo 181, Japan
Li, J., Metcalf, T. R., Canfield, R. C., Wülser, J. P., & Kosugi, T. 1997, ApJ, 482, 490
Masuda, S., Kosugi, T., Hara, H., Tsuneta, S., & Ogawara, Y. 1994, Nature, 371, 495
Matsushita, K., Masuda, S., Kosugi, T., Inda, M., & Yaji, K. 1992, PASJ, 44, L89
Nishio, M., Yaji, K., Kosugi, T., Nakajima, H., & Sakurai, T. 1997, ApJ, 489, 976
Nitta, N., Dennis, B. R., & Kiplinger, A. L. 1990, ApJ, 353, 313
Press, W. H., Flannery, B. P., Teukolsky, S. A., & Vetterling, W. T. 1986, Numerical Recipes, The Art of Scientific Computing (Cambridge: Cambridge Univ. Press)
Sakao, T. 1994, Ph.D. Thesis, Natl. Astron. Obs., Mitaka, Tokyo
Sakao, T., Kosugi, T., & Masuda, S. 1998, in Observational Plasma Astrophysics: Five Years of *Yohkoh* and Beyond, ed. T. Watanabe, T. Kosugi, & A. C. Sterling (Dordrecht: Kluwer), 273
Sato, J., Kosugi, T., & Makishima, K. 1999, PASJ, in press
Wang, H., Gary, D. E., Zirin, H., Schwartz, R. A., Sakao, T., Kosugi, T., & Shibata, K. 1995, ApJ, 453, 505